



# Mechanical Properties and Microstructure of a High-Power Laser-Welded Ti6Al4V Titanium Alloy

Zhen Chen, Bingfeng Wang, and Bohua Duan

(Submitted July 23, 2019; in revised form December 1, 2019; published online March 16, 2020)

In this study, the high-power solid-state laser was used to weld the Ti6Al4V titanium alloy plates with a thickness of 8 mm. Microstructure and mechanical properties of the high-power laser-welded Ti6Al4V titanium alloy were investigated by the optical microscope, electron probe microanalysis, transmission electron microscope and nanoindentation technique. According to our findings, the average tensile strength of the joint is higher than 957 MPa, and the fusion zone possesses the highest microhardness in the laser-welded Ti6Al4V titanium alloy. The content of aluminum is reduced in the fusion zone. Equiaxed  $\alpha + \beta$  phases in the fusion zone are transformed into columnar  $\beta$  and acicular  $\alpha'$  martensite grains by the martensitic transformation. Dynamic recrystallization of acicular  $\alpha'$  martensite occurs at the edge of columnar  $\beta$  grains. Additionally, due to the extremely fast cooling rate and the shock of the laser, the crystal nucleus undergoes a phase transformation to form a staggered martensite structure. Meanwhile, ultrafine grains and nanograins formed at the martensite crossing are also preserved. The results of nanoindentation reveal that the fine acicular  $\alpha'$  martensite phase improves the creep resistance of the fusion zone.

**Keywords** laser welding, mechanical properties, microstructure, titanium alloy

## 1. Introduction

The Ti6Al4V titanium alloy is a typical  $\alpha$ - $\beta$  titanium alloy containing 6%  $\alpha$ -stabilizing element aluminum (Al) and 4%  $\beta$ -stabilizing element vanadium (V). It possesses the advantages of high specific strength and excellent corrosion resistance with wide application in aerospace and medical fields (Ref 1-3). The working principle is to stimulate the gas or the solid crystal to produce the high-energy laser for laser welding conduction heating, and thus there is a rapid rise in temperatures above the melting point, and simultaneously rapid cooling rate creates a metallurgical bond (Ref 4, 5). In addition, it is a solid joining process with a large depth-to-width ratio of the welding seam, a narrow heat-affected zone and minimal deformation of welding parts (Ref 6). Due to its unique characteristics, it has been widely applied in the aerospace, automotive and steel industries (Ref 4, 7, 8). A study on the microstructure and mechanical properties of the laser-welded joint can help to strengthen the application and improve the performance of the laser weld technology and can also comprehend the microstructural response of the materials under the high-energy laser welding.

Numerous studies are available on the relationship among laser welding parameters, microstructure and performance of the materials. Fuerschbach et al. (Ref 9) used the weld area algorithm to link

the material properties and welding process parameters with the laser energy conversion rate, obtaining the empirical relationship between CO<sub>2</sub> and yttrium-aluminum-garnet (YAG) laser welding process parameters, which can be applied to steel and titanium alloy. Mehrpouya et al. (Ref 10) studied the influence of the main process parameters of laser welding on weld formation, demonstrating that the welding parameters could be efficaciously controlled by adjusting the process parameters such as laser power, welding speed and defocusing distance, hence improving the welded joint quality. Hong (Ref 11) and Liu et al. (Ref 12) employed the finite element simulation method to investigate the temperature field of laser-welded Ti6Al4V titanium alloy plate microhardness model of the welding seam and residual stress distribution, laying a theoretical basis and a reference for the microstructure evolution in Ti6Al4V titanium alloy under laser welding. Cheng et al. (Ref 13) and Chen et al. (Ref 14) reported that the laser-welded Ti6Al4V titanium alloy had sound mechanical properties, and the tensile strength was superior to the base metal due to basket-weave microstructure with acicular martensite  $\alpha'$  in the large columnar crystal in the joint. Ahn et al. (Ref 15) and Akman et al. (Ref 16) studied the influence of welding parameters on the size and orientation of the laser-welded Ti6Al4V titanium alloy. It was deduced that the low heat input could result in smaller weld bead grains and smaller acicular martensite  $\alpha'$ , while grains were easily enlarged at high heat input and the secondary  $\alpha$  phase appeared on the grain boundary.

The present study aims to investigate the mechanical properties of the high-power laser-welded Ti6Al4V titanium alloy joint, to study mechanical properties and microstructure of the fusion zone in the joint and to discuss the formation of the microstructure in the Ti6Al4V titanium alloy under high-power laser welding.

## 2. Materials and Experiments

The material used in the current work is the Ti6Al4V titanium alloy plate with a size of 8 mm (thickness)  $\times$  100 mm (width)  $\times$  1000 mm (length). The laser welding was carried

Zhen Chen and Bohua Duan, School of Materials Science and Engineering, Central South University, Changsha 410083, People's Republic of China; and Bingfeng Wang, State Key Laboratory for Powder Metallurgy, Central South University, Changsha 410083, People's Republic of China; and School of Materials Science and Engineering, Central South University, Changsha 410083, People's Republic of China. Contact e-mail: wangbingfeng@csu.edu.cn.

out with a YLS10000 fiber laser manufactured by American IPG Company. The laser power, the defocusing amount and the laser spot moving rate were 2.2 kW, + 2 mm and 1 m/min, respectively. Before the welding, the surface of the sample was machined into a smooth surface. Shielding gas such as argon was used to prevent oxidation during welding, with a flow rate of 30-40 L/min.

The tensile strength was measured to verify the weld quality, and the tensile samples were tested at room temperature on the universal tensile tester (INSTRON 5569, made in America) at a loading speed of 1 mm/min. The microstructure of the welded joint was observed using the optical microscope (XJZ-A2, made in China), the electron probe microanalysis (JXA-8230, made in Japan) and the transmission electron microscope (Tecnai G2 Spirit TWIN, FEI, made in America). The electrolytic double-spray formulation used in the transmission electron microscope was 5% perchloric acid + 35% *n*-butanol + 60% methanol. The microhardness of the base metal (BM), heat-affected zone (HAZ) and fusion zone (FZ) was measured by the microhardness tester (Shimadzu, MHV-2T, made in Japan). The load and the loading time were 50 g and 10 s, respectively. To study mechanical properties of superfine structure in the welded joint, nanoindentation tests were performed at room temperature utilizing a nanoindenter (CSM, MCT + UNHT, Switzerland) equipped with a diamond Berkovich indenter. The maximum load and load holding time were 10 mN and 60 s, respectively.

### 3. Results and Discussion

#### 3.1 Microstructure and Mechanical Properties of Laser-Welded Joints

The tensile strength of the laser-welded Ti6Al4V titanium alloy is over 957 MPa, and the samples are broken at the base metal near the joint, as shown in Fig. 1. Therefore, the strength of the laser-welded joint is greater than that of the base metal.

Figure 2 presents the cross-sectional optical micrographs of the welded joint, showing that the joint consists of three parts, that is, the fusion zone (FZ), the heat-affected zone (HAZ) and the base metal (BM). The weld depth is 3.2 mm, and it is

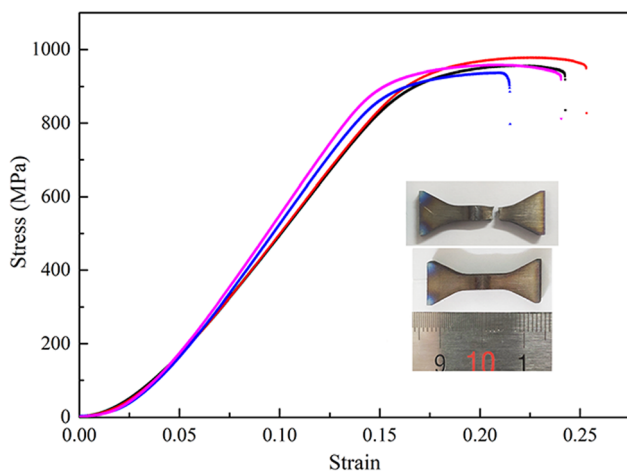


Fig. 1 Tensile stress vs. strain curve

evenly divided into top, middle and bottom parts to facilitate discussion. In the BM, the  $\alpha$  phase is distributed on the  $\beta$  phase substrate, as shown in Fig. 2(b). The interdigitated acicular  $\alpha'$  martensites in the columnar  $\beta$  grains formed at a high temperature can be observed in the upper part of the FZ, as shown in Fig. 2(c). The formation of the acicular martensite is related to hydrogenation in the Ti6Al4V titanium alloy and is also associated with a decrease in the critical cooling rate for martensitic formation (Ref 17). The grain size in the bottom of the FZ is smaller than that in the upper part, with a negligible amount of interdigitated acicular  $\alpha'$ , as demonstrated in Fig. 2(d). HAZ consists of residual  $\alpha$  phase and acicular martensites as shown in Fig. 2(e).

Figure 3 depicts the microhardness distribution in the laser-welded Ti6Al4V titanium alloy joint. The microhardness is measured at the upper, middle and bottom of the joint. The average microhardness in the FZ is nearly 372 HV, and the microhardness in the BM is significantly lower than that in the FZ and HAZ. The microhardness decreases rapidly from FZ to HAZ.

In order to confirm the distribution of elements in the joint, the map element scanned results are shown in Fig. 4. The content of Al and V in the BM is relatively higher, in comparison with FZ which is depleted of Al. During the cooling stage, the relative content of the V augments will reduce the likelihood of  $\beta$  phase transforming to  $\alpha'$  martensite phase, which will increase the brittleness and reduce the plasticity of the joint.

Bright-field electron images of the BM and FZ are shown in Fig. 5 and 6, respectively. BM consists of equiaxed polygon  $\beta$  and  $\alpha$  phase. The microstructure of the hexagonal close-packed acicular  $\alpha'$  martensite in FZ is revealed in Fig. 6(a) and (c), respectively. These acicular  $\alpha'$  martensites with disparate scales are intersected with each other. The length of the normally growing acicular martensite is tens of microns indicated by a blue dotted line in Fig. 6(c). Owing to the action of the molten pool stirring, the primary acicular martensites are broken and new martensites are produced with a length of 1 micron indicated by the yellow dotted line in Fig. 6(c). These martensites intersect with the normally growing martensite. Additionally, the secondary martensite with a length of only tens of nanometers was also distributed between the normally growing acicular martensites represented by the dotted red line in Fig. 6(c). Equiaxed ultrafine grains and nanograins are formed at the intersections of the acicular martensites, as shown in Fig. 6(b) and (d), respectively.

Figure 7 shows the nanoindentation results in the laser-welded Ti6Al4V titanium alloy joint. The morphology of indentation is reflected in Fig. 7(a). The sizes of the indentation are around 2  $\mu$ m. The load-displacement and the creep displacement curves of the Ti6Al4V titanium alloy in FZ, HAZ and BM at constant strain rate are displayed in Fig. 7(b) and (d), separately. The average value of the nanohardness of the acicular  $\alpha'$  martensite in the fusion zone is about 5.38 GPa, which is much higher than that of the  $\beta$  and  $\alpha$  phase in HAZ and BM, as shown in Fig. 7(c). There are three stages during the nanoindentation test, consisting of loading, holding and unloading. During the loading stage, the applied load in the ultrafine grains in the fusion zone is greater than that for grains in HAZ and BM under constant displacement. In the holding time, the value of creep displacement for the acicular  $\alpha'$  martensite in the FZ is the smallest, indicating that the creep resistance of the acicular  $\alpha'$  martensite is better than that in the



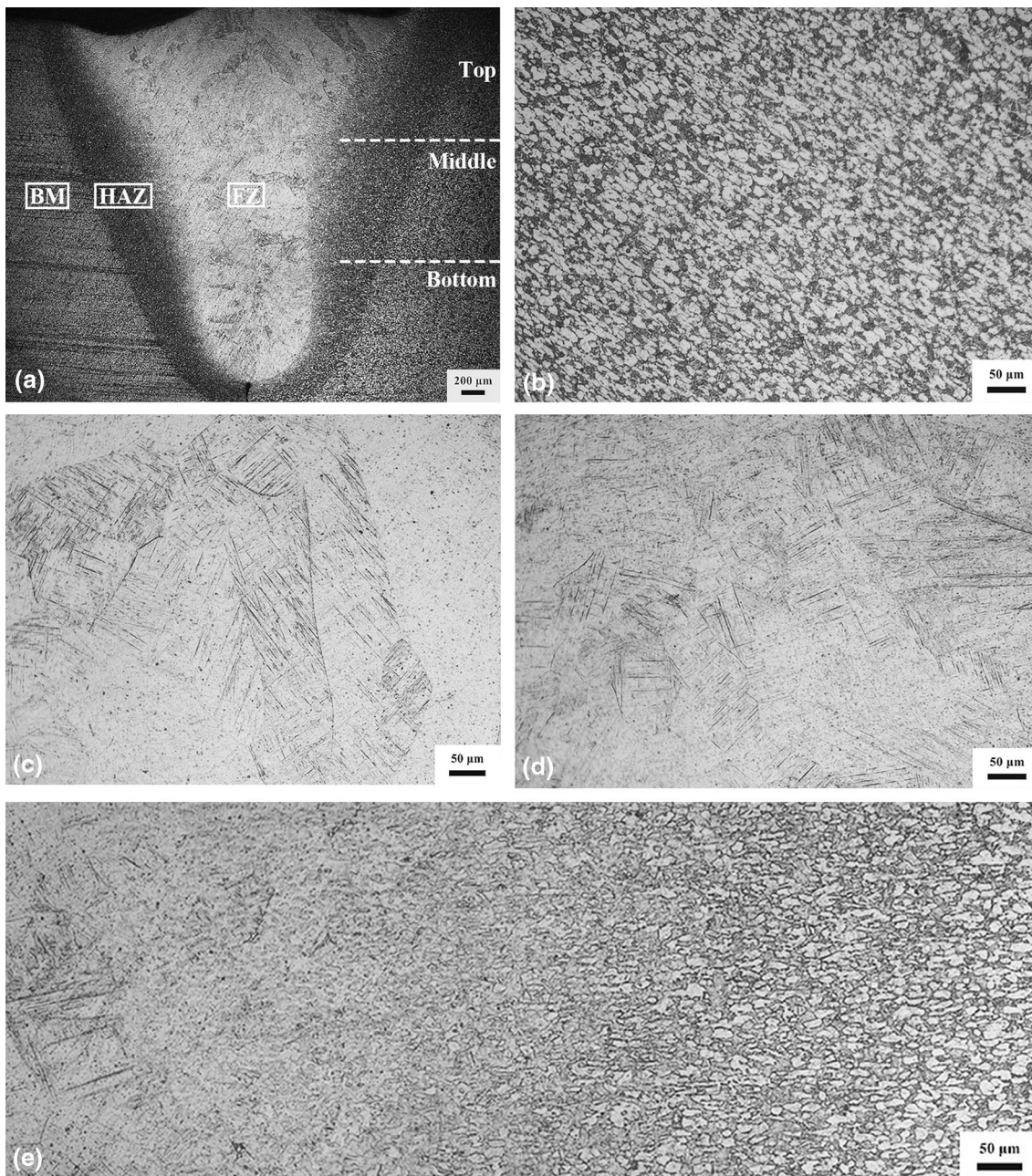


**Fig. 2** Optical micrograph of laser-welded joint. (a) Whole joint. (b) BM. (c) Up part of the FZ. (d) Down part of the FZ. (e) HAZ

$\beta$  and  $\alpha$  phase. We investigated a queue of nanoindentation in the FZ with the constant strain rate and loads. The load–displacement curves and the creep displacement curves of the Ti6Al4V titanium alloy in the FZ are shown in Fig. 7(e) and (f), respectively. By reason of the measuring error, the actual loads are slightly larger than 10 mN. These testing results can be split into two types, which is type I and type II for primary and secondary acicular  $\alpha'$  martensites, respectively, as shown in Fig. 6(c), respectively. The slope of the type I in the creep displacement curve is slightly higher than that of the type II. Hence, the acicular  $\alpha'$  martensites in the fusion zone have significant reinforcement, and the primary acicular  $\alpha'$  martensites have lower strength and better plasticity.

### 3.2 Calculation of Temperature Field in the Fusion Zone

During laser welding, a small hole effect occurs at the welded joint, which differs from the welding characteristics of tungsten inert gas (TIG), friction stir welding (FSW), etc. The high energy rate laser irradiates and heats the metal surface to a temperature above the melting point in a very short time. The escaping steam and the impact of the laser shock make additional pressure on the liquid metal below, causing the metal in the molten pool to sink downward and form holes. Svenungsson et al. (Ref 18) introduced the fundamental principles of the laser welding process and the physical model of a small hole formation and the welding pool dynamics



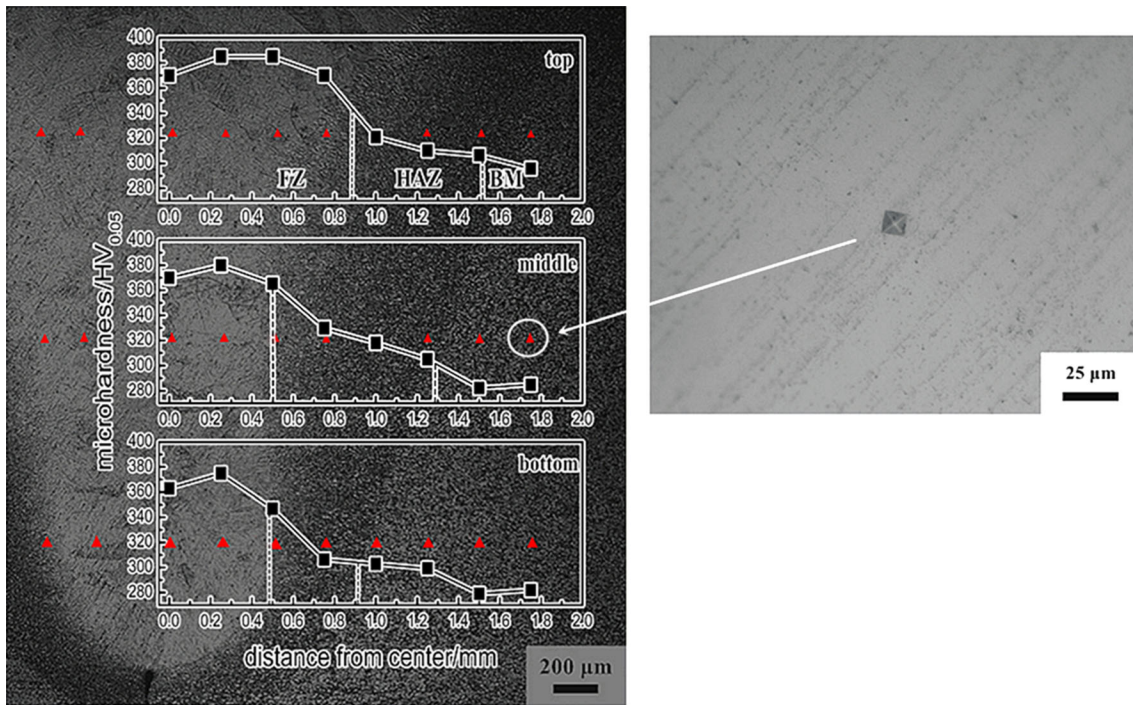


**Fig. 3** Microhardness of the laser-welded joint

during laser welding. The principal modeling methods for energy transfer from the laser beam to the surface of the holes and fluid flow in the material were discussed elsewhere. The shape of the small holes directly affects the temperature distribution of the weld. The schematic of the small hole model is shown in Fig. 8. The mean widths of the fusion zone and the heat-affected zone are used to establish the temperature field, and the common traits of high-energy welding are utilized. The temperature field at the joint can be expressed by the following expression (Ref 19):

$$T(x, t) = \frac{(T_{\max} - T_0) \cdot \delta}{\sqrt{4\pi kt_T}} \cdot \exp\left(-\frac{x^2}{4kt_T}\right) \quad (\text{Eq 1})$$

$$\delta = \frac{\delta_1}{2} + \delta_2 \quad (\text{Eq 2})$$

where  $k$ ,  $x$  and  $t_T$  are the diffusion coefficient, the distance from the HAZ to the center of the FZ and the heat transfer time, respectively.  $T_{\max}$  and  $T_0$  are the maximum temperature and room temperature, respectively.  $\delta_1$  and  $\delta_2$  are the average widths of the FZ and HAZ accordingly.  $T_0$  is 298 K (25 °C);  $\delta_1$  is 1200  $\mu\text{m}$ ; and  $\delta_2$  is 700  $\mu\text{m}$ . The parameter  $t_T$  is expressed as follows:

$$t_T = \frac{x^2}{2k} \quad (\text{Eq 3})$$

The temperature of the Ti6Al4V titanium alloy in the fusion zone can be calculated as follows:

$$T = \frac{(T_{\max} - 298)}{\sqrt{2\pi}} \cdot e^{-0.5} \cdot \frac{0.0013}{x} \quad (x \geq 600 \mu\text{m}). \quad (\text{Eq 4})$$

When  $x$  is 600  $\mu\text{m}$ ,  $T$  is 1941 K (1668 °C), so the  $T_{\max}$  in the melt is 4000 K (3727 °C).

$$T = \frac{1.16442}{x} \quad (\text{Eq 5})$$

The cooling rate can be obtained by the following expression:

$$T(0, t) = T_m \cdot \sqrt{\frac{t_r}{t}} \quad (t > t_r) \quad (\text{Eq 6})$$

where  $t_r$  is the time when the wave returns to the surface.  $T$ ,  $T_m$  and  $t$  are the temperature, the melting point and the time, respectively. The parameter  $t_r$  can be expressed by the following expression:

$$t_r = 2H/C_0 \quad (\text{Eq 7})$$

where  $H$  is the distance from the center of the fusion zone to the surface and  $C_0$  is the volume velocity. Here,  $H$  is 2 mm;  $T_m$  is 1941 K (1668 °C); and  $C_0$  is 6150 m/s.

Therefore, the cooling rate can be expressed as follows:

$$T(0, t) = 1.565 \cdot t^{-\frac{1}{2}} \quad (t > 0.852 \mu\text{s}). \quad (\text{Eq 8})$$

The temperature versus distance and the temperature versus time curves can be obtained by Eq 5 and 8, respectively, as shown in Fig. 9. When the distance from the center is greater than 600  $\mu\text{m}$ , the temperature descends dramatically as the distance increases. During laser welding, the temperature is close to 895 K (622 °C, 0.46  $T_m$ ) at a distance of about 1500  $\mu\text{m}$  near the base metal. Consequently, the temperature in the FZ is enough to facilitate the phase transformation of the titanium alloy, and grains in HAZ close to FZ can be recrystallized. Besides, during the cooling stage (0.85-30  $\mu\text{s}$ ), the average cooling rate of FZ is about  $4.84 \times 10^7$  k/s. Therefore, the grains do not grow during the cooling stage; nanograins and martensites in the FZ are retained.

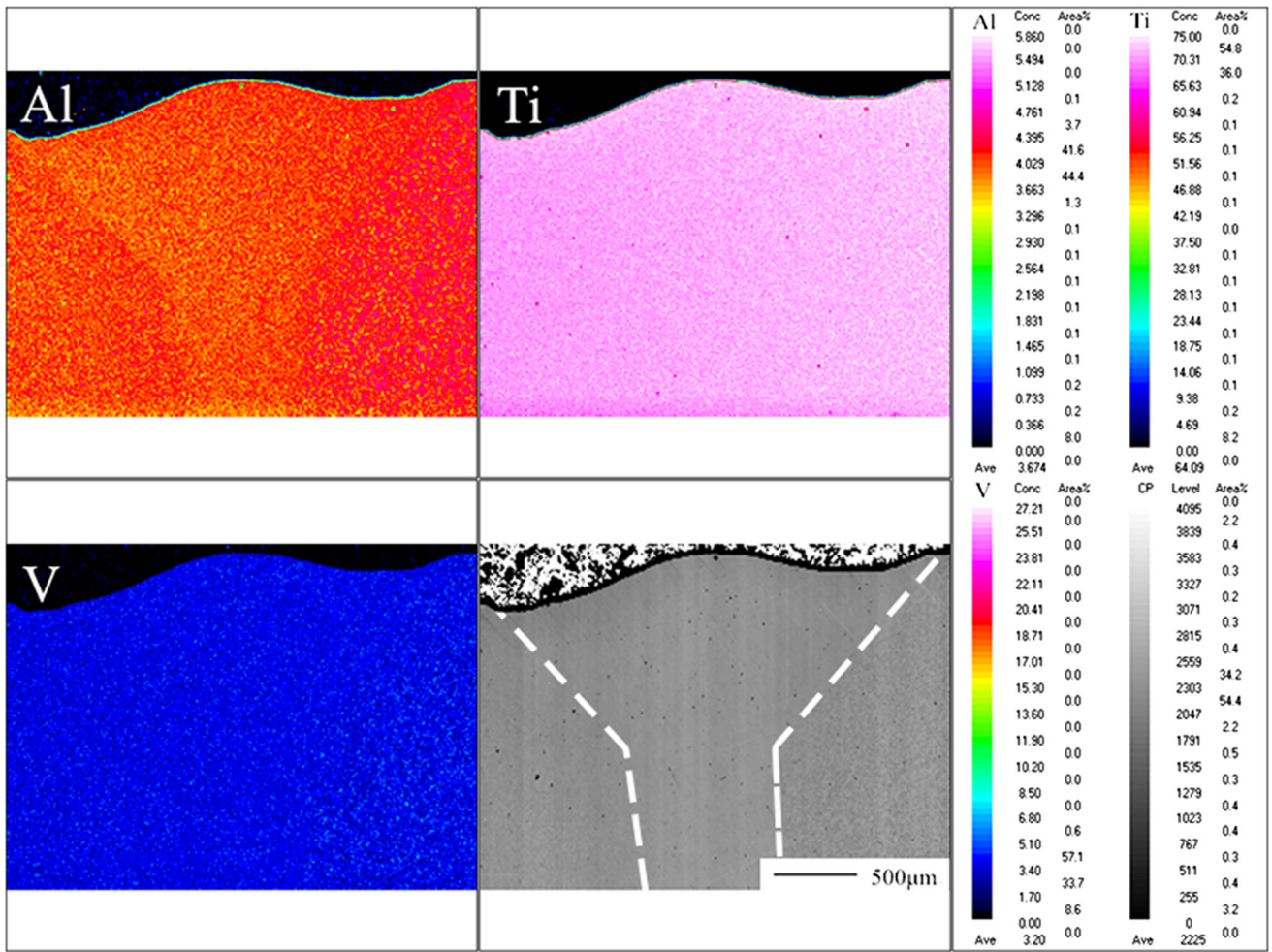


Fig. 4 EPMA map analysis results of laser-welded joint

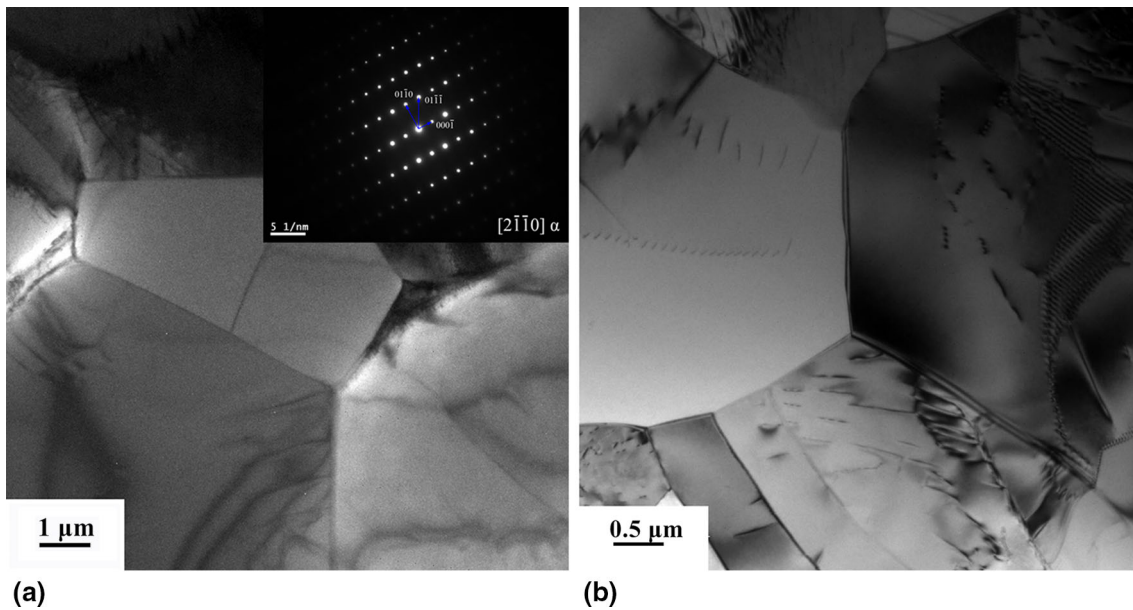
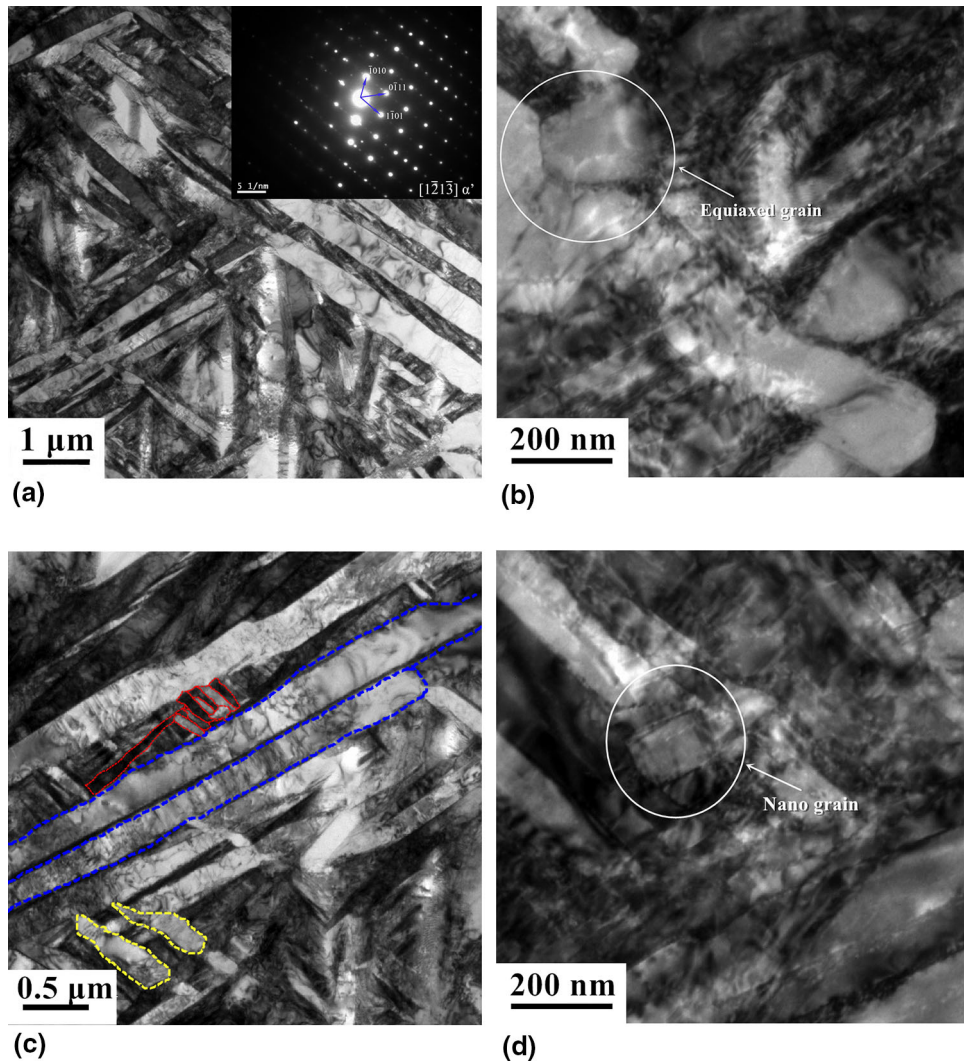


Fig. 5 Bright-field electron images of BM. (a) Polygonization of grains. (b) High angle of grain boundaries



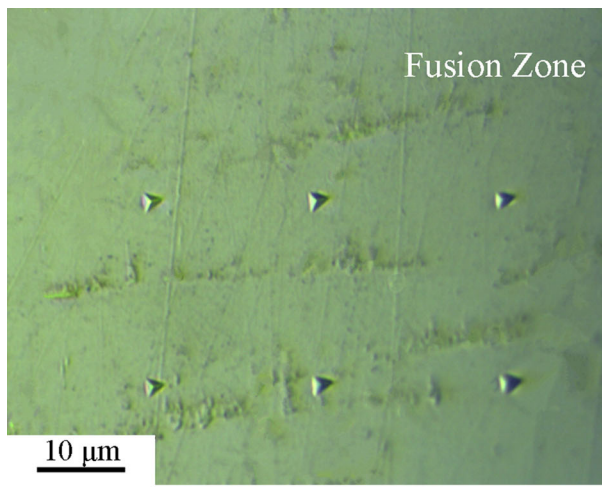


**Fig. 6** Bright-field electron images of FZ. (a) Acicular  $\alpha'$  martensite laths. (b) Equiaxed ultrafine grain. (c) Intersection of acicular  $\alpha'$  martensite laths. (d) Nanograins

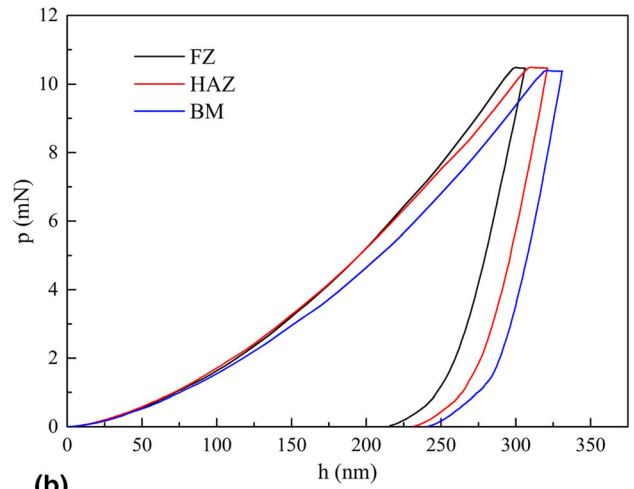
### 3.3 Formation of the Microstructure in the Fusion Zone

For laser welding, not only does the high temperature affect the transformation of the microstructure in FZ, but also the high strain rate conditions caused by the laser play a vital role (Ref 20). Matsumoto et al. (Ref 21) found that at higher strain, the main microstructure of discontinuous dynamic recrystallization alters the transition state from the  $\alpha + \beta$  phase to the acicular  $\alpha'$  martensite. Based on the above analysis of mechanical properties and microstructure in FZ, the formation of the FZ can be described as follows in Fig. 10. The  $\alpha$  phase is distributed on the  $\beta$  phase substrate in the initial state (a). At the beginning of the laser welding, the temperature exceeds the  $\beta$  transus temperature, and the  $\alpha$  phase turned into the  $\beta$  phase. Because the plasma jet and high-energy wave propagation in the laser welding process exacerbate the stirring effect of the

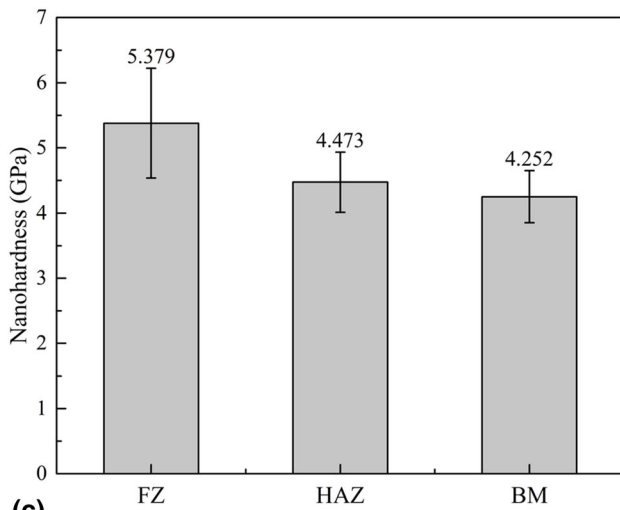
FZ, the thermal expansion of the material in the high-temperature area is restrained by the surrounding material. The acicular  $\alpha'$  martensite nucleates at the  $\beta$  phase boundary (b). Once the crystal nucleus is formed, it is rapidly transformed into the primary acicular  $\alpha'$  martensite by shear phase transformation (c). With the action of the molten pool stirring, the primary acicular  $\alpha'$  martensites are broken and intersected with one another, as shown in Fig. 6(c). There are nucleation and growth of secondary  $\alpha'$  martensites on the primary acicular  $\alpha'$  martensite grain boundary. Meanwhile, the intersecting martensites are easy to nucleate. Finally, due to the rapid cooling rate, nanocrystalline grains and martensites are retained (d). Therefore, the formation of the microstructure in FZ is the result of the high temperature and the laser shocking during laser welding.



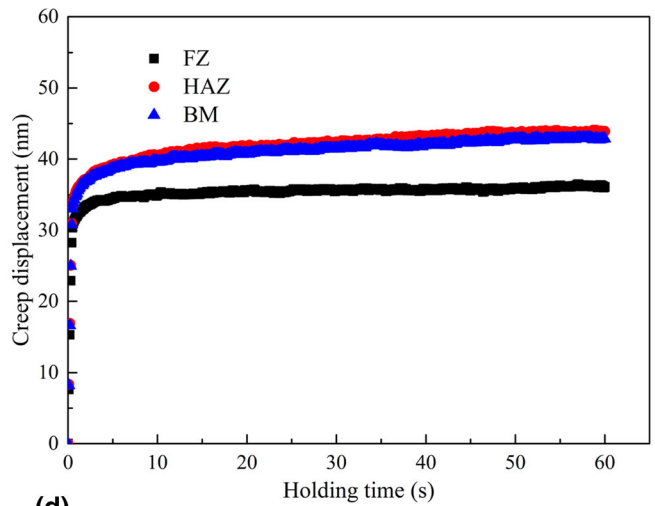
(a)



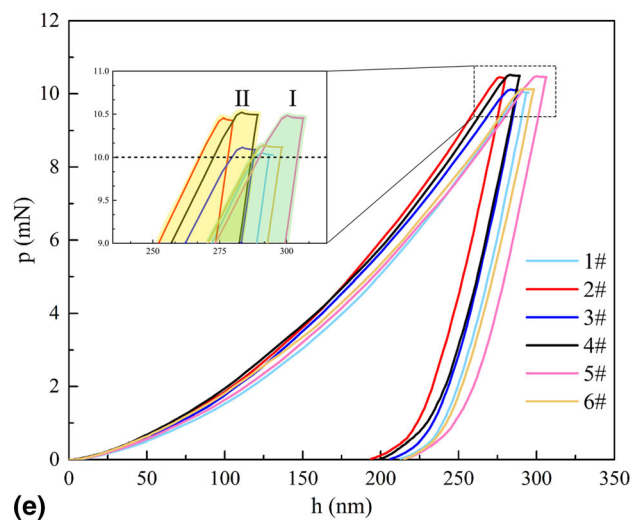
(b)



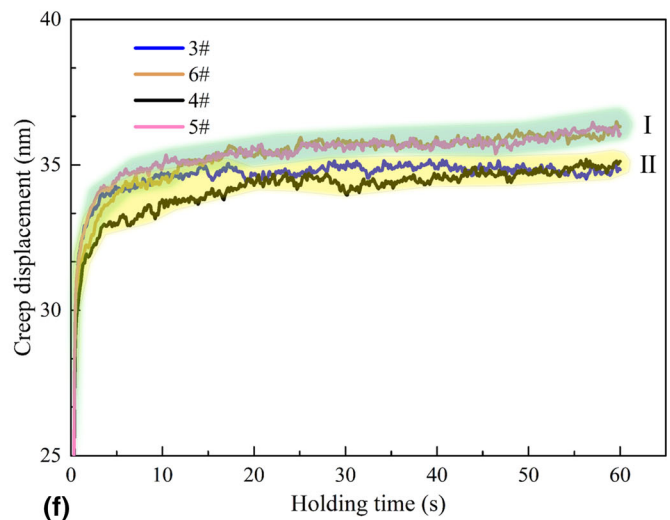
(c)



(d)



(e)



(f)

**Fig. 7** Nanoindentation analysis of the laser-welded joint loaded at a strain rate of  $0.5 \text{ s}^{-1}$ . (a) Scanning electron micrograph of indentations loaded at 10 mN. (b) Load vs. displacement curves. (c) Nanohardness. (d) Creep displacements during the holding stage. (e) Load vs. displacement curves (1#, 5# and 6# are type I; 2#, 3# and 4# are type II). (f) Creep displacements for acicular  $\alpha'$  martensites. (5# and 6# are type I; 3# and 4# are type II)

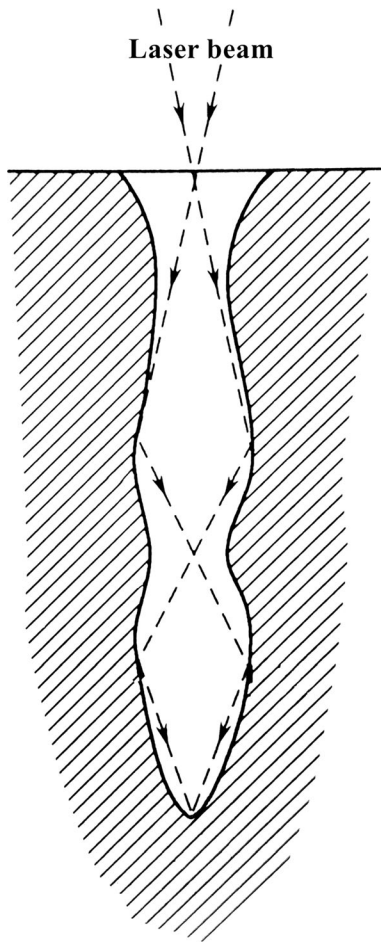


**Fig. 8** Schematic of the laser beaming process

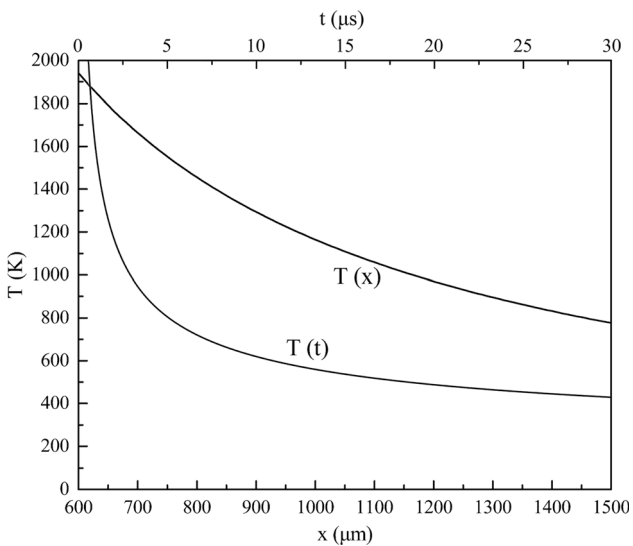


**Fig. 9** Temperature vs. distance and temperature vs. time curves

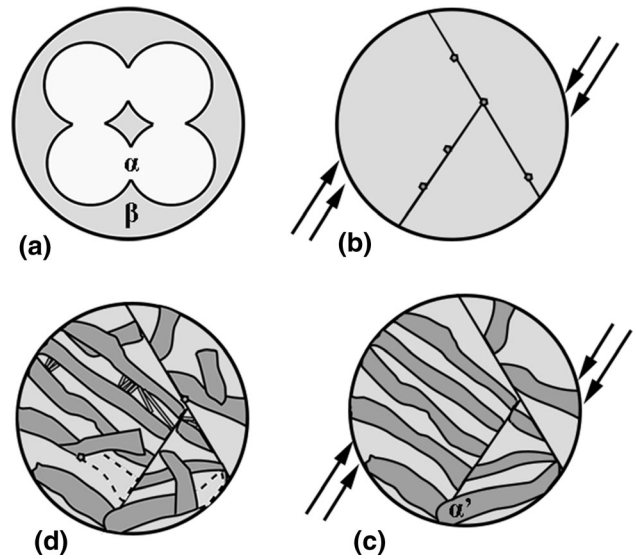


**Fig. 10** Schematic of microstructure evolution in the FZ. (a) Initial microstructure. (b) Shear impact deformation and rearrangement of the grain boundary. (c)  $\alpha'$  martensite phase transformation. (d) Intersection of the  $\alpha'$  martensite laths

## 4. Conclusions

The average tensile strength for the high-power laser-welded Ti6Al4V titanium alloy is greater than 957 MPa, and samples are broken at the base metal near the joint. The average microhardness in FZ is much higher than that in BM and HAZ. The reduction of Al in the fusion zone decreases the stability of the  $\alpha$  phase. The FZ is composed of the acicular  $\alpha'$  martensite and the columnar  $\beta$  phase. The acicular  $\alpha'$  martensites with disparate scales are intersected with each other. Equiaxed ultrafine grains and nanograins are formed at the intersections of the acicular  $\alpha'$  martensites. The nanoindentation results show that the acicular  $\alpha'$  martensite in the FZ has a significant reinforcement in the hardness. Compared with the secondary acicular  $\alpha'$  martensites, the primary acicular  $\alpha'$  martensites have lower strength and better plasticity.

## Acknowledgments

This work was financially supported by the National Natural Science of China (No. 51771231), the Scientific and Technological Innovation Projects of Hunan Province, China (No. 2017GK2292), and the State Key Laboratory of Powder Metallurgy, Central South University, Changsha, China, Grant Number 20181106. The authors wish to express their most sincere gratitude to Professor M. A. Meyers at the University of California, San Diego, for his advice and help.



## References

1. M.W. Turner, P.L. Crouse, L. Li, and A.J.E. Smith, Investigation Into CO<sub>2</sub> Laser Cleaning of Titanium Alloys for Gas-Turbine Component Manufacture, *Appl. Surf. Sci.*, 2006, **252**(13), p 4798–4802. <https://doi.org/10.1016/j.apsusc.2005.06.061>
2. X. Li, S. Hu, J. Xiao, and L. Ji, Effects of the Heterogeneity in the Electron Beam Welded Joint on Fatigue Crack Growth in Ti-6Al-4V Alloy, *Mater. Sci. Eng. A*, 2011, **529**, p 170–176. <https://doi.org/10.1016/j.msea.2011.09.014>
3. S. Wang and X. Wu, Investigation on the Microstructure and Mechanical Properties of Ti-6Al-4V Alloy Joints with Electron Beam Welding, *Mater. Des.*, 2012, **36**, p 663–670. <https://doi.org/10.1016/j.matdes.2011.11.068>
4. Y.W. Ai, P. Jiang, C.M. Wang, G.Y. Mi, S.N. Geng, W. Liu, and C. Han, Investigation of the Humping Formation in the High Power and High-Speed Laser Welding, *Opt. Laser Eng.*, 2018, **107**, p 102–111. <https://doi.org/10.1016/j.optlaseng.2018.03.010>
5. X. Cao, M. Jahazi, J.P. Immarigeon, and W. Wallace, A Review of Laser Welding Techniques for Magnesium Alloys, *J. Mater. Process. Technol.*, 2006, **171**(2), p 188–204. <https://doi.org/10.1016/j.jmatprotec.2005.06.068>
6. A. Haboudou, P. Peyre, A.B. Vannes, and G. Peix, Reduction of Porosity Content Generated During Nd: YAG Laser Welding of A356 and AA5083 Aluminium Alloys, *Mater. Sci. Eng. A*, 2003, **363**(1–2), p 40–52. [https://doi.org/10.1016/s0921-5093\(03\)00637-3](https://doi.org/10.1016/s0921-5093(03)00637-3)
7. K.M. Hong and Y.C. Shin, Prospects of Laser Welding Technology in the Automotive Industry: A Review, *J. Mater. Process. Technol.*, 2017, **245**, p 46–69. <https://doi.org/10.1016/j.jmatprotec.2017.02.008>
8. G. Sierra, P. Peyre, F. Deschaux-Beaume, D. Stuart, and G. Fras, Steel to Aluminium Key-Hole Laser Welding, *Mater. Sci. Eng. A*, 2007, **447**(1–2), p 197–208. <https://doi.org/10.1016/j.msea.2006.10.106>
9. P.W. Fuerschbach and G.R. Eisler, Effect of Laser Spot Weld Energy and Duration on Melting and Absorption, *Sci. Technol. Weld. Join.*, 2013, **7**(4), p 241–246. <https://doi.org/10.1179/136217102225004293>
10. M. Mehrpouya, A. Gisario, A. Brotzu, and S. Natali, Laser Welding of NiTi Shape Memory Sheets Using a Diode Laser, *Opt. Laser Technol.*, 2018, **108**, p 142–149. <https://doi.org/10.1016/j.optlastec.2018.06.038>
11. K.M. Hong, Analysis of Microstructure and Mechanical Properties Change in Laser Welding of Ti6Al4V with a Multiphysics Prediction Model, *J. Mater. Process. Technol.*, 2016, **237**, p 420–429. <https://doi.org/10.1016/j.jmatprotec.2016.06.034>
12. C. Liu, J.X. Zhang, and J. Niu, Numerical and Experimental Analysis of Residual Stresses in Full-Penetration Laser Beam Welding of Ti6Al4V Alloy, *Rare. Met. Mater. Eng.*, 2009, **38**(8), p 1317–1320. [https://doi.org/10.1016/s1875-5372\(10\)60066-5](https://doi.org/10.1016/s1875-5372(10)60066-5)
13. D.H. Cheng, J.H. Huang, X.K. Zhao, and H. Zhang, Microstructure and Superplasticity of Laser Welded Ti-6Al-4V Alloy, *Mater. Des.*, 2009, **30**(1), p 103–106. <https://doi.org/10.1016/j.matdes.2009.06.020>
14. S.H. Chen, J.H. Huang, D.H. Cheng, H. Zhang, and X.K. Zhao, Superplastic Deformation Mechanism and Mechanical Behavior of a Laser-Welded Ti-6Al-4V Alloy Joint, *Mater. Sci. Eng. A*, 2012, **541**, p 110–119. <https://doi.org/10.1016/j.msea.2012.02.011>
15. J. Ahn, L. Chen, C.M. Davies, and J.P. Dear, Parametric Optimisation and Microstructural Analysis on High Power Yb-Fibre Laser Welding of Ti-6Al-4V, *Opt. Laser Eng.*, 2016, **86**, p 156–171. <https://doi.org/10.1016/j.optlaseng.2016.06.002>
16. E. Akman, A. Demir, T. Canel, and T. Sınmazçelik, Laser Welding of Ti6Al4V Titanium Alloys, *J. Mater. Process. Technol.*, 2009, **209**(8), p 3705–3713. <https://doi.org/10.1016/10.1016/j.jmatprotec.2008.08.026>
17. H.J. Liu, L. Zhou, and Q.W. Liu, Microstructural Evolution Mechanism of Hydrogenated Ti-6Al-4V in the Friction Stir Welding and Post-weld Dehydrogenation Process, *Scr. Mater.*, 2009, **61**(11), p 1008–1011. <https://doi.org/10.1016/j.scriptamat.2009.08.012>
18. J. Svenungsson, I. Choquet, and A.F.H. Kaplan, Laser Welding Process—A Review of Keyhole Welding Modelling, *Physics Procedia.*, 2015, **78**, p 182–191. <https://doi.org/10.1016/j.phpro.2015.11.042>
19. B.F. Wang, X.Z. Luo, S. Zhao, and F.Y. Xie, Microstructure and Its Formation Mechanism in the Interface of Ti/NiCr Explosive Cladding Bar, *J. Mater. Eng. Perform.*, 2015, **24**(2), p 1050–1058. <https://doi.org/10.1007/s11665-014-1321-0>
20. M.J. Zhang, G.Y. Chen, Y. Zhou, S.C. Li, and H. Deng, Observation of Spatter Formation Mechanisms in High-Power Fiber Laser Welding of Thick Plate, *Appl. Surf. Sci.*, 2013, **280**(1), p 868–875. <https://doi.org/10.1016/j.apsusc.2013.05.081>
21. H. Matsumoto, B. Liu, S.H. Lee, Y.P. Li, Y. Ono, and A. Chiba, Frequent Occurrence of Discontinuous Dynamic Recrystallization in Ti-6Al-4V Alloy with  $\alpha'$  Martensite Starting Microstructure, *Metall. Mater. Trans. A*, 2013, **44**(7), p 3245–3260. <https://doi.org/10.1007/s11661-013-1655-5>

**Publisher's Note** Springer Nature remains neutral with regard to jurisdictional claims in published maps and institutional affiliations.